International Forum on Aeroelasticity and Structural Dynamics
IFASD 2024
17-21 June 2024, The Hague, The Netherlands

DOUBLET LATTICE MODELING AND ANALYSIS OF UNSTEADY AERODYNAMIC EFFECTS FOR A FLEXIBLE UNMANNED AIRCRAFT DURING MANEUVERS AND GUST ENCOUNTERS

Leif Rieck[1], **Benjamin Herrmann**[1], **Frank Thielecke**[1]

[1]Institute of Aircraft Systems Engineering, Hamburg University of Technology
Nesspriel 5, 21129 Hamburg, Germany
leif.rieck@tuhh.de
benjamin.herrmann@tuhh.de
frank.thielecke@tuhh.de

Keywords: Unsteady Aerodynamics, UAV, Doublet Lattice Method, Aeroelasticity

Abstract: This paper presents the modeling and analysis of unsteady aerodynamics for a slightly flexible $25\,\mathrm{kg}$ unmanned aircraft during maneuvers and gust encounters. The unsteady model is based on a doublet lattice method (DLM) implemented in MATLAB. It is combined with an existing high-fidelity quasi-steady aerodynamics model derived from system identification using flight test data. Utilizing the physical rational function approximation, it is possible to differentiate between the steady and unsteady components of the DLM. Consequently, the steady component of the DLM can be replaced by the high-fidelity model such that quasi-steady and unsteady DLM forces and moments are superimposed. The combined unsteady aerodynamics are integrated with linear structural dynamics identified from ground vibration tests and nonlinear equations of motion based on the practical mean-axes formulation. Simulation studies are conducted to analyze the impact of unsteady aerodynamic effects on the flexible aircraft. The results indicate that unsteady effects, while noticeable during rapid maneuvers in the aeroelastic frequency range, are especially significant when considering high-frequency control surface deflections and encounters with short gusts. The proposed modeling approach successfully combines high-fidelity quasi-steady aerodynamics with unsteady DLM aerodynamics, demonstrating validity across a wide range of reduced frequencies.

1 INTRODUCTION

Future efficient aircraft designs will consider high aspect ratio wings and lightweight structures. This leads to more flexible wings which exhibit increased in-flight deformations and structural vibrations affecting the flow characteristics around the lifting surfaces. These time-varying effects can become especially relevant during rapid maneuvers and gust encounters. This work aims to analyze the impact of such unsteady aerodynamic effects on the flight dynamics of a slightly flexible 25kg unmanned aircraft.

There are various methods for the purpose of modeling unsteady aerodynamics for flexible aircraft ranging from strip theory indicial function approaches based on Wagner and Küssner functions [1, 2] to high-fidelity computational fluid dynamics methods [3, 4]. The latter's application for flight dynamic simulations and controller design is often limited by their complexity, leading to extensive computational effort and high-order models. Extended strip theory based on indicial functions, on the other hand, is a well-known approach to model unsteady effects

based on potential flow theory [5–8]. Recent applications include models for handling quality investigations of a flexible airliner [9], comparisons with flight test data for a slightly flexible utility aircraft [10], and a gust load alleviation simulation environment [11].
While extended strip theory offers a computationally efficient framework with moderate modeling effort, it is generally deemed a low-fidelity approach. A middle ground between fidelity and modeling complexity, especially for low-speed applications, is offered by potential flow panel methods. The most prevalent approach for unsteady aerodynamics is the doublet lattice method (DLM) often casually described as an unsteady extension of the vortex lattice method (VLM). Since its first implementation in 1969 [12], numerous refinements have been made [13–16]. Nowadays, the DLM is considered an established tool in research and industry alike. Its improved accuracy compared to indicial functions for gust loads analysis has been shown in [17]. The DLM is widely used for flight dynamics and loads investigations [18, 19], and it has been applied to the aeroelastic modeling of unmanned flexible aircraft in recent years [20–23].
Given a suitable model for unsteady aerodynamics, it is of interest to evaluate the impact of unsteady effects on the flight dynamic behavior. In [10], the indicial function method was considered integral to capture the aeroelastic dynamics of the slightly flexible aircraft investigated therein. On the other hand, a negligible impact of unsteady aerodynamics on flutter speed predictions was reported in [24] for a body-freedom flutter demonstrator.

This paper aims to extend an existing high-fidelity quasi-steady aerodynamics model, derived from system identification, to include unsteady aerodynamics. An unsteady DLM model is implemented in MATLAB/SIMULINK and combined with the quasi-steady high-fidelity model by exploiting the structure of the physical rational function approximation [18]. Thus, the steady component of the DLM model can be replaced by the high-fidelity quasi-steady model. This combined aerodynamic model is integrated with linear structural and rigid-body dynamics, as well as several other subsystem-models of actuators, sensors, and filters to obtain a nonlinear flight dynamic simulation model. To ensure consistency of the combined quasi-steady and unsteady models, the parameters of the quasi-steady aerodynamics model are newly adapted during a parameter estimation. Further, comparisons of quasi-steady and unsteady simulations are presented to evaluate the impact of unsteady aerodynamic effects. In the simulations, the aircraft dynamics are excited with maneuvers at various frequencies ranging from fast rigid-body dynamics to the aeroelastic frequency range as well as high-frequency gusts.
This paper is organized as follows. Section 2 introduces the slightly flexible $25\,\mathrm{kg}$ unmanned aircraft G-Flights Dimona and its structural characteristics. The modeling framework is presented in section 3. Therein, the model structure, the equations of motion, the aerodynamic models, and the combination of the quasi-steady and unsteady aerodynamics are described. Finally, the results of the parameter identification and the simulation studies are presented in section 4.

2 UNMANNED TEST AIRCRAFT G-FLIGHTS DIMONA

The G-Flights Dimona, depicted in Figure 1, serves as a test and research aircraft for the development and validation of modeling [25, 26], loads estimation [27], and control [28] methods for flexible aircraft. It is an unmanned replica of the *HK36 Super Dimona* at a scale of 1:3 with a total mass of $25\,\mathrm{kg}$. The aircraft is driven by an electric motor with a maximum power of $4\,\mathrm{kW}$ and has a length of $2.4\,\mathrm{m}$. The original wings have been replaced by a pair with increased flexibility and structure-integrated sensors. They have a span of $5.4\,\mathrm{m}$ and a surface area of $1.6\,\mathrm{m}^2$. The aircraft comprises a total of 11 control surfaces: Two elevators, one rudder, four ailerons, and four flaperons. It is further equipped with several industry-grade sensors and computers for

Figure 1: G-Flights Dimona

guidance, navigation, and control (GNC) applications. Strain gauges for shear, bending, and torison as well as intertial measurement units (IMUs) are located at relevant stations along the fuselage, empennage, and wings. With wing tip deformations of up to 10% of the half-span at $2g$, it is considered a slightly flexible aircraft in accordance with [29].
Assuming linear structural dynamics, the elastic deformation is represented by a set of free vibration modes and mode shapes. Ground vibration tests (GVT) with hammer and shaker inputs as well as a modal analysis were performed to determine the structural modes from experimental data. The first seven modes were identified and considered for the structural dynamics model. Details on the measurement setup, test execution, and results are presented in [30]. The structural mode shapes were subsequently determined from a finite element (FE) model that was adapted to match the GVT data. These modes are listed in Table 1 with their respective frequency f and modal damping ξ. They are visualized in Figure 2. Due to its low natural frequency, the first symmetric wing bending is the mode most likely to affect the flight dynamics. Additionally, it is the only mode with a natural frequency below the actuator bandwidth of 6.74Hz. Hence, it is considered to be the most relevant structural mode.

Table 1: First seven structural modes of the G-Flights Dimona

Mode	Description	f [Hz]	ξ [%]
1	First symmetric wing bending	3.97	0.85
2	First antisymmetric wing bending	8.56	1.38
3	First antisymmetric vertical tailplane bending	11.18	1.24
4	First symmetric in-plane wing bending	13.21	1.83
5	Second symmetric wing bending	14.60	1.79
6	First symmetric horizontal tailplane bending	17.24	2.76
7	First symmetric wing torsion	25.83	1.91

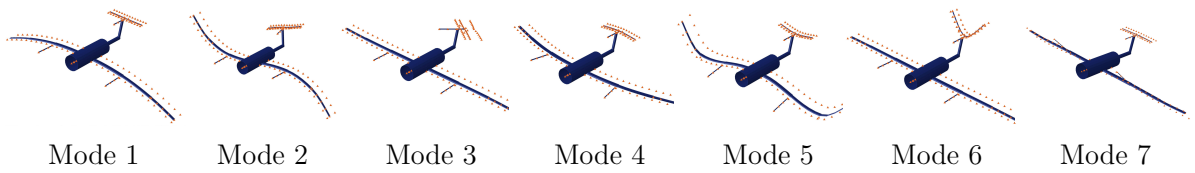

Figure 2: Visualization of the structural modes

3 FLEXIBLE AIRCRAFT MODEL

The nonlinear simulation model is implemented in MATLAB/SIMULINK and follows the modular subsystem-based modeling approach of the in-house library FLYSIM. The implementation of the unsteady DLM model in the nonlinear simulation model is shown in Figure 3. The ac-

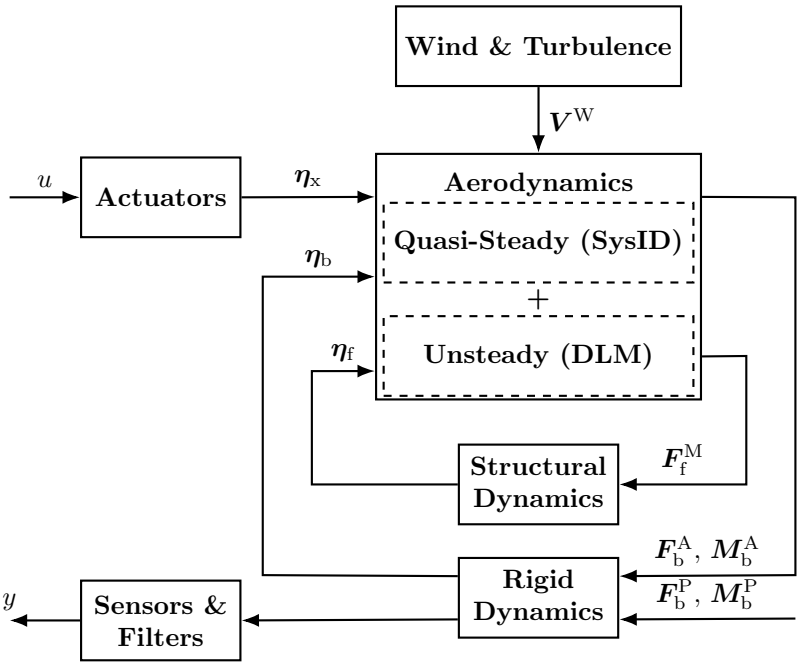

Figure 3: Implementation of the unsteady DLM model in the nonlinear simulation model

tuators are modeled by second-order systems of the identified servo actuator dynamics. The aerodynamics consist of a high-fidelity quasi-steady model based on strip theory and system identification. In this work, it is combined with an unsteady DLM model. Making use of the physical rational function approximation [18], it is possible to differentiate between steady and unsteady components of the aerodynamic forces and moments computed by the DLM. Hence, only the unsteady components are computed and superimposed with the quasi-steady model at each strip. Additionally, atmospheric disturbances are modeled by the wind & turbulence subsystem. The resulting forces and moments are inputs for the linear structural dynamics and the nonlinear rigid-body dynamics. These dynamics are described by the equations of motion in the mean axes body reference frame based on [31]. Lastly, the outputs are obtained from sensor and filter models. The full aircraft model comprises additional subsystems for the propulsion system, landing gear, as well as earth and atmosphere.

3.1 Equations of Motion

The equations of motion describe the aircraft's response to external forces and moments considering nonlinear rigid-body dynamics and linear structural dynamics. They are developed with the choice of the body reference frame to satisfy the practical mean axes constraints of zero translational and linear rotational momentum due to elastic deformations [31]. This is achieved by representing the elastic deformation in terms of free vibration modes and locating the origin of the body reference frame O_{b} at the instantaneous center of mass, see Figure 4. The position $\boldsymbol{r}_i$ of a mass element $\mathrm{d}m_i$ of the flexible aircraft in an inertial reference frame O_I can be expressed in terms of the relative position $\boldsymbol{p}_i$ to this body reference frame and the position $\boldsymbol{r}_0$ of the origin of O_{b}: $\boldsymbol{r}_i = \boldsymbol{r}_0 + \boldsymbol{p}_i$. With the free vibration modes, the elastic deformations of the n_{g} structural nodes $\boldsymbol{d}_{\mathrm{g}}$ can be written as a multiplication of the flexible modal matrix $\boldsymbol{\Phi}_{\mathrm{gf}}$ and

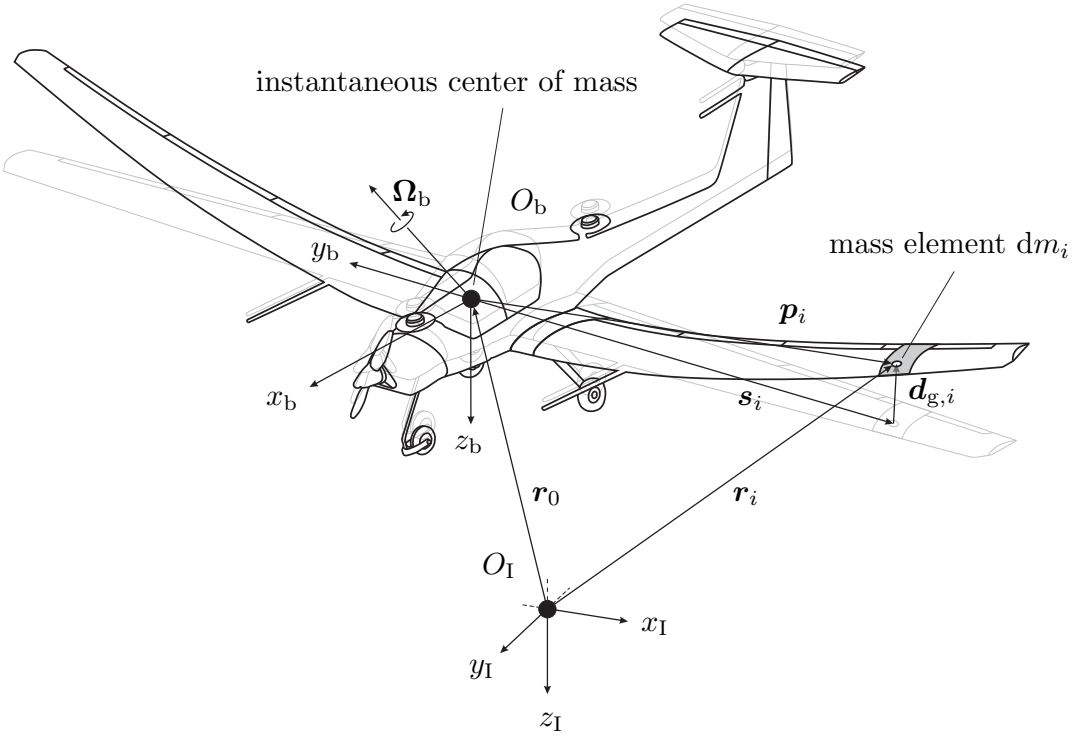

Figure 4: Visualization of the elastic deformation and definition of the reference frames

the modal coordinates $\boldsymbol{\eta}_\mathrm{f}$

$$\boldsymbol{d}_\mathrm{g} = \begin{bmatrix} \boldsymbol{d}_1 \\ \vdots \\ \boldsymbol{d}_{n_\mathrm{g}} \end{bmatrix}_\mathrm{g} = \boldsymbol{\Phi}_\mathrm{gf}\, \boldsymbol{\eta}_\mathrm{f}\,. \tag{1}$$

Then, the position $\boldsymbol{p}_i$ of the mass element can be separated into its undeformed part $\boldsymbol{s}_i$ and its deformed part $\boldsymbol{d}_{\mathrm{g},i}$: $\boldsymbol{p}_i = \boldsymbol{s}_i + \boldsymbol{d}_{\mathrm{g},i}$. The equations of motion can be derived in O_b by assuming a structure of lumped masses, small deformations, collinear deformations and deformation rates, and a constant tensor of inertia:

$$m\,\left(\dot{\boldsymbol{V}}_\mathrm{b} + \boldsymbol{\Omega}_\mathrm{b} \times \boldsymbol{V}_\mathrm{b} - \boldsymbol{T}_\mathrm{bI}\,\boldsymbol{g}_\mathrm{I}\right) = \boldsymbol{F}_\mathrm{b}^\mathrm{E}, \tag{2}$$

$$\boldsymbol{J}\,\dot{\boldsymbol{\Omega}}_\mathrm{b} + \boldsymbol{\Omega}_\mathrm{b} \times \boldsymbol{J}\,\boldsymbol{\Omega}_\mathrm{b} = \boldsymbol{M}_\mathrm{b}^\mathrm{E}, \tag{3}$$

$$\boldsymbol{M}_\mathrm{ff}\,\ddot{\boldsymbol{\eta}}_\mathrm{f} + \boldsymbol{B}_\mathrm{ff}\,\dot{\boldsymbol{\eta}}_\mathrm{f} + \boldsymbol{K}_\mathrm{ff}\,\boldsymbol{\eta}_\mathrm{f} = \boldsymbol{F}_\mathrm{f}^\mathrm{M} \tag{4}$$

Equation 2 and Equation 3 describe the nonlinear translational and rotational rigid-body flight dynamics in the body reference frame, respectively. The vector $\boldsymbol{V}_\mathrm{b}$ contains the translational velocities and $\boldsymbol{\Omega}_\mathrm{b}$ is the vector of angular velocities. The aircraft's mass is denoted by m and its inertia tensor by $\boldsymbol{J}$. The matrix $\boldsymbol{T}_\mathrm{bI}$ transforms the gravitational acceleration vector $\boldsymbol{g}_I$ from the inertial to the body-reference frame. The external forces from aerodynamics and propulsion are denoted as $\boldsymbol{F}_\mathrm{b}^\mathrm{E}$ and the resulting moments as $\boldsymbol{M}_\mathrm{b}^\mathrm{E}$. Equation 4 represents the linear differential equations of the structural dynamics. Here, $\boldsymbol{M}_\mathrm{ff}$, $\boldsymbol{B}_\mathrm{ff}$, and $\boldsymbol{K}_\mathrm{ff}$ are the modal mass, damping, and stiffness matrices, respectively. The modal forces are denoted as $\boldsymbol{F}_\mathrm{f}^\mathrm{M}$. The nonlinear rigid-body dynamics and the linear structural dynamics are coupled due to the aerodynamic forces.

3.2 Quasi-Steady Strip Aerodynamics Model

The quasi-steady aerodynamics are modeled using a stability and control derivative approach and by applying strip theory. The underlying aerodynamic parameters have been previously

identified from flight test data as described in [26].

In strip theory, the lifting surfaces are divided into n_{strips} spanwise strips, each with local width b_i, local chord c_i, and local surface area S_i. Each strip corresponds to precisely one structural node (g). The elastic deformation is thus known from the superposition of mode shapes and model coordinates, see Equation 1. Furthermore, each strip is assigned a neutral point (n) at the quarter-chord position and a zero pressure point (p) at the mid-chord position. They act as reference points for the aerodynamic forces and moments. The positions of these points are depicted in Figure 5. The orientation of each neutral point, zero pressure point, and structural

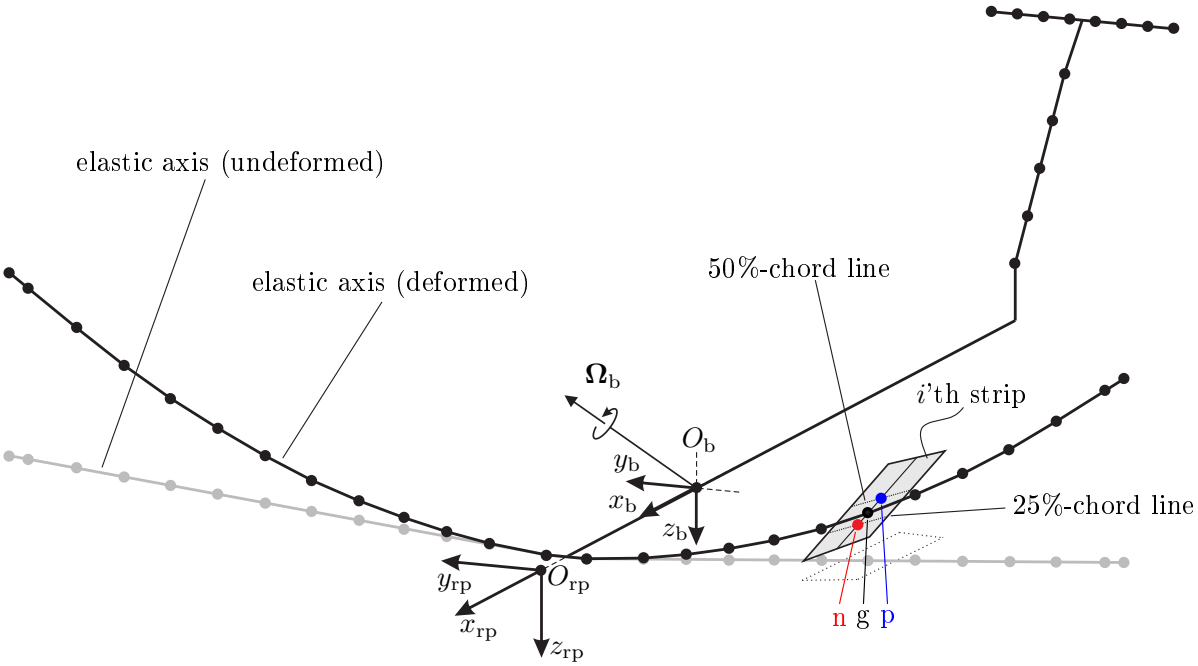

Figure 5: Position of the i'th strip relative to the reference point frame O_{rp} and the body reference frame O_{b}

node can be described relative to a body-fixed frame, which has its origin at the reference point O_{rp}. It is aligned with the body reference frame O_{b}, but translated to the origin of the wing by a vector $\boldsymbol{b}_{\text{cm}}$, which is considered constant due to the assumption of small deformations. Neglecting chord-wise deformation of the strips, the instantaneous position of the i'th neutral point relative to the reference point frame is given by

$$\boldsymbol{b}_{\text{n},i} = \boldsymbol{b}^{\text{r}}_{\text{n},i} + \boldsymbol{d}^{\text{t}}_{\text{g},i} + \boldsymbol{T}_{\text{ng},i}\left(\boldsymbol{b}^{\text{r}}_{\text{n},i} - \boldsymbol{b}^{\text{r}}_{\text{g},i}\right) \tag{5}$$

with the rigid position vector $\boldsymbol{b}^{\text{r}}_{\text{n},i}$, the translational elastic deformations $\boldsymbol{d}^{\text{t}}_{\text{g},i}$, and the transformation matrix $\boldsymbol{T}_{\text{ng},i}$ from the i'th structural node to the i'th neutral point due to elastic rotations. The positions of the zero pressure point and the structural node can be described similarly.
The quasi-steady aerodynamics of each strip are described by a local non-dimensional lift and a local non-dimensional drag coefficient. They are formed from the well-known stability and control derivatives normalized by ${}^{S_i}/_{S_{\text{ref}}}$:

$$C_{L,i} = C_{L_0,i} + C_{L_\alpha,i} \cdot \left(\frac{1+\sqrt{X_{0,i}}}{2}\right) \cdot \alpha_{\text{eff},i} + \sum_{i_{\text{x}}=1}^{n_{\text{x}}} C_{L_{\eta_{\text{x},i_{\text{x}}},i}} \cdot \eta_{\text{x},i_{\text{x}}} \tag{6}$$

$$C_{D,i} = C_{D_0,i} + k_i \cdot C^2_{L,i} \tag{7}$$

Here, quasi-steady stall effects are modeled by an approximation of the steady flow-separation point $X_{0,i}$ based on Kirchhoff's flow separation theory [32]. For vertical stabilizer strips, the lift coefficient is interpreted as a side force coefficient $C_{Y,i}$ with the effective angle $\beta_{\text{eff},i}$. All terms are assumed to act on the strip's neutral point, except for $C_{L_0,i}$ and $C_{L_{\eta_{\text{x},i_\text{x}}},i} \cdot \eta_{\text{x},i_\text{x}}$, which are assumed to act on the strip's zero pressure point and a variable point along the centerline as a function of the deflection [33], respectively. They are transferred to the strip's neutral point and the resulting moments are described in terms of non-dimensional moment coefficients $C_{l,i}$ (roll), $C_{m,i}$ (pitch), and $C_{n,i}$ (yaw). Non-dimensionality is achieved through dividing the moments by $\overline{s}$ (roll, yaw) and $\overline{c}$ (pitch), respectively. Lastly, the aerodynamic characteristics of the fuselage are modeled by additional non-dimensional one-point stability derivatives.

The local relative flow at each strip is determined by summing the velocity components of aerodynamic free stream, aerodynamic rotation about the body reference frame, elastic translation, and wind

$$\boldsymbol{V}_{\text{n},i} = \boldsymbol{T}_{\text{nb,i}} \left(\boldsymbol{V}_{\text{b}}^{\text{A}} + \boldsymbol{\Omega}_{b}^{\text{A}} \times (\boldsymbol{b}_{\text{n},i} - \boldsymbol{b}_{\text{cm}}) \right) + \dot{\boldsymbol{d}}_{\text{g},i}^{\text{t}} + \boldsymbol{V}_{\text{n},i}^{\text{W}} \,, \tag{8}$$

where $\boldsymbol{T}_{\text{nb,i}}$ denotes the transformation matrix from the body reference frame to the i'th neutral point due to rigid and elastic dihedral, twist, and sweep. The velocity components due to elastic rotations are neglected.
Downwash at the tailplane strips is modeled by the induced downwash angle $\epsilon_{T,i}$. It is used to correct the local relative flow at the tailplane strips. The angle depends on the angle of attack and flaperon deflections, delayed by the time $\Delta t_{\epsilon_T,i}$ the flow requires to reach the tailplane strips [34]

$$\epsilon_{T,i}(t) = \frac{\partial \epsilon_T}{\partial \alpha} \cdot \alpha(t - \Delta t_{\epsilon_T,i}) + \sum_{i_\text{f}=1}^{n_\text{f}} \frac{\partial \epsilon_T}{\partial \eta_{\text{x},i_\text{f}}} \cdot \eta_{\text{x},i_\text{f}}(t - \Delta t_{\epsilon_T,i}) \,, \tag{9}$$

where $\partial\epsilon_T/\partial\alpha$ and $\partial\epsilon_T/\eta_{\text{x},i_\text{f}}$ denote the partial derivatives of the downwash angle w.r.t. the angle of attack and flaperon deflections, respectively.
The effective angle of attack and angle of sidelip of each strip are obtained based on the local relative flow of Equation 8, which is corrected by the induced downwash angle for the tailplane strips

$$\alpha_{\text{eff},i} = \arctan\left(\frac{w_{\text{n},i}}{u_{\text{n},i}}\right), \qquad \beta_{\text{eff},i} = \arcsin\left(\frac{v_{\text{n},i}}{|\boldsymbol{V}_{\text{n},i}|}\right) . \tag{10}$$

These effective strip angles and the control surface deflections are used to compute the coefficient vectors $\boldsymbol{C}_{\text{n},i}^{F}$ and $\boldsymbol{C}_{\text{n},i}^{M}$. The resulting quasi-steady aerodynamic loads $\boldsymbol{P}_{\text{n},i}^{\text{A,qs}}$ (forces and moments) acting at the i'th neutral point are then given by

$$\boldsymbol{P}_{\text{n},i}^{\text{A,qs}} \begin{cases} \boldsymbol{F}_{\text{n},i}^{\text{A,qs}} = \bar{q}_{\text{eff},i}\, S_{\text{ref}}\, \boldsymbol{C}_{\text{n},i}^{F} \\ \boldsymbol{M}_{\text{n},i}^{\text{A,qs}} = \bar{q}_{\text{eff},i}\, S_{\text{ref}}\, \boldsymbol{E}\, \boldsymbol{C}_{\text{n},i}^{M} \,, \end{cases} \tag{11}$$

where $\boldsymbol{E}$ is a diagonal matrix with main diagonal elements $\{\bar{s},\, \bar{c},\, \bar{s}\}$ and $\bar{q}_{\text{n},i}$ denotes the effective dynamic pressure at each strip.

Initial distributions of the stability and control derivatives were obtained from VLM calculations. They were subsequently adapted based on flight test data using the output error method in the time domain and maximum likelihood estimation. Details can be found in [26].

3.3 Unsteady Doublet Lattice Aerodynamics Model

In this section, the implementation of a Doublet Lattice Method in MATLAB/SIMULINK to determine the distributed unsteady forces and moments is described. The implementation is based on previous work by [20] and follows the approach of [18]. The governing equations and their derivations are available in the literature and will not be described here in detail.
The DLM is a linear potential-flow based panel method that allows to determine the pressure distribution of a lifting surface undergoing oscillations of a certain frequency [12]. The wings and the tailplane are treated as flat mean surfaces and small deformations are assumed. The lifting surfaces are divided into a finite number of trapezoidal panels with a constant pressure distribution for each. The resulting grid for the G-Flights Dimona, its coordinate system, and the index notation for each panel are depicted in Figure 6. Note that the x- and z-axis are inverted compared to the body-fixed frame defined in subsection 3.2[1]. Following the notation of [18], l

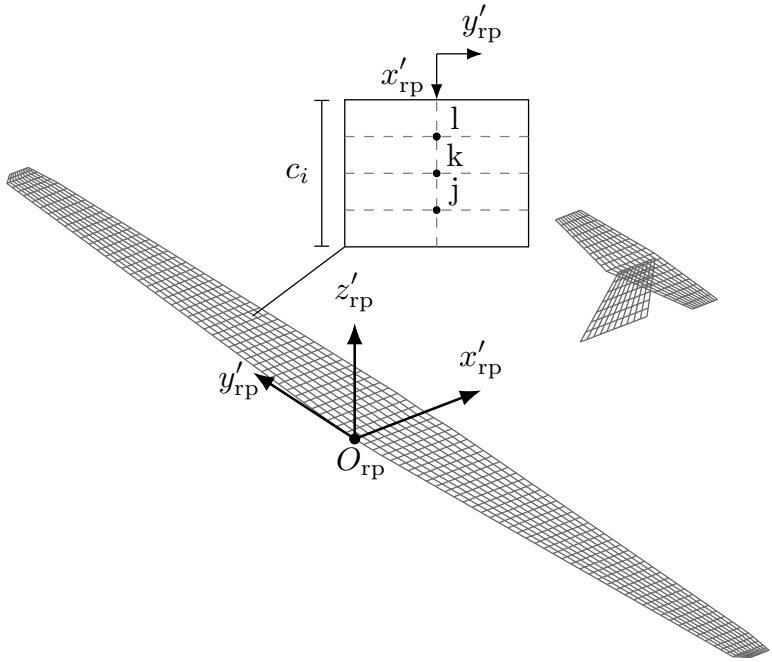

Figure 6: DLM grid of the G-Flights Dimona and the corresponding notation

denotes the load acting point (quarter chord), k is the panel reference point (mid chord), and j denotes the collocation point (three-quarter chord).
By numerically integrating the Kernel function, the frequency-dependent matrix of aerodynamic influence coefficients (AIC-matrix) $\boldsymbol{Q}_{\mathrm{jj}}(k)$ is obtained. It relates a downwash distribution $\boldsymbol{w}_{\mathrm{j}}$ to a resulting pressure distribution

$$\Delta \boldsymbol{c}_{p\mathrm{j}}(k) = \boldsymbol{Q}_{\mathrm{jj}}(k)\, \boldsymbol{w}_{\mathrm{j}}(k)\,. \tag{12}$$

The reduced frequency

$$k = \frac{\bar{c}}{2\, V_{\mathrm{TAS}}}\, \omega \tag{13}$$

is an indicator for the unsteadiness of the flow and depends on the mean aerodynamic chord $\bar{c}$, the airspeed V_{TAS}, and the oscillation frequency ω. For the G-Flights Dimona, eight reduced

[1] Signs are adjusted where appropriate.

frequencies up to $k = 3$ were considered. Usually, the solution for the steady case $k = 0$ is replaced by a VLM solution to avoid approximation errors. Similarly, the steady aerodynamics in this work are represented by the high-fidelity model described in subsection 3.2. Implementation details are given in subsection 3.4.

Modeling the fluid structure interaction between the aerodynamic panel midpoints k and the structural nodes g is required to account for the influence of the flexible aircraft's elastic deformation on the aerodynamic properties. As is conventional, the two degrees of freedom z-translation and pitch about the y-axis are considered for each panel. Meanwhile, three degrees of freedom are considered for each structural node[2]: z-translation, roll about its x-axis, and pitch about its y-axis. For the i'th panel or node, respectively, this is denoted as

$$\boldsymbol{d}_{\mathrm{k},i} = \begin{bmatrix} z & \theta \end{bmatrix}^{\mathsf{T}}_{\mathrm{k},i} ; \; \boldsymbol{d}_{\mathrm{g},i} = \begin{bmatrix} z & \phi & \theta \end{bmatrix}^{\mathsf{T}}_{\mathrm{g},i} . \tag{14}$$

For the purpose of fluid structure interaction, a transformation matrix $\boldsymbol{T}_{\mathrm{kg}}$ based on spline interpolation is constructed. Thus, the deformations of the structural grid can be mapped onto the aerodynamic grid

$$\boldsymbol{d}_{\mathrm{k}} = \boldsymbol{T}_{\mathrm{kg}} \, \boldsymbol{d}_{\mathrm{g}} \tag{15}$$

and similarly, assuming structural equivalence [35], aerodynamic loads can be mapped onto the structural nodes

$$\boldsymbol{P}^{\mathrm{A}}_{\mathrm{g}} = \boldsymbol{T}^{\mathsf{T}}_{\mathrm{kg}} \, \boldsymbol{P}^{\mathrm{A}}_{\mathrm{k}} . \tag{16}$$

Here, $\boldsymbol{P}$ denotes the loads acting at each node or panel, respectively. Note that $\boldsymbol{P}^{\mathrm{A}}_{\mathrm{g}}$ consists of one local force and two moments, while $\boldsymbol{P}^{\mathrm{A}}_{\mathrm{k}}$ consists of only one force and one moment at each panel due to the degrees of freedom, see Equation 14.
The transformation between these grids is achieved by making use of an intermediate spline grid as proposed in [20]. Hence, two consecutive transformations are required. First, a transformation from the structural nodes g to the spline nodes s is performed with $\boldsymbol{T}_{\mathrm{sg}}$. Second, the deformations of the aerodynamic grid are obtained by interpolating between the deformations of the spline nodes with $\boldsymbol{T}_{\mathrm{ks}}$. Thus, the overall transformation is defined as

$$\boldsymbol{T}_{\mathrm{kg}} = \boldsymbol{T}_{\mathrm{ks}} \, \boldsymbol{T}_{\mathrm{sg}} . \tag{17}$$

The spline grid spans the lifting surface and subsequently allows for the interpolation of local deformations based on thin plate theory. Since this approach assumes deformations only normal to the surface, each spline node has only a single heave degree of freedom $z_{s,i}$. The corresponding grid is obtained by projecting the structural nodes to the leading and trailing edges of the lifting surfaces as shown in Figure 7. The three degrees of freedom of each structural node can now be transformed into pure heaving motion of the corresponding three spline nodes (considering the structural node itself as a spline node) through the utilization of a small angle approximation as described in [36]. This yields the transformation matrix $\boldsymbol{T}_{\mathrm{sg}}$. The second transformation matrix is obtained based on surface spline theory. Given the known spline node deformations, the unknown displacements at the panel midpoints are determined using thin plate deformation equations. For this purpose, infinite plate splines based on radial basis functions are implemented as described in [35, 37], yielding $\boldsymbol{T}_{\mathrm{ks}}$.

The aerodynamic boundary conditions are determined with the so-called differentiation matrices $\boldsymbol{D}^1_{\mathrm{jk}}$ and $\boldsymbol{D}^2_{\mathrm{jk}}$ [18]. They relate the displacements of the aerodynamic panels in terms of their

[2]Note that $\boldsymbol{\Phi}_{\mathrm{gf}}$ in subsection 3.2 denotes a modal matrix with six degrees of freedom for each node.

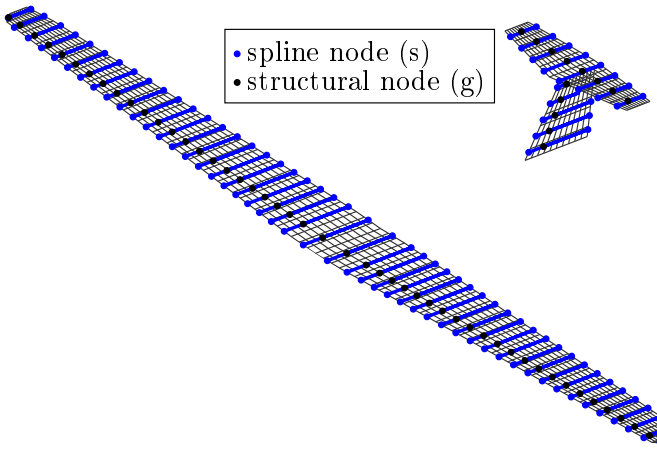

Figure 7: Spline grid of the G-Flights Dimona

heaving and pitching motion at the panel midpoint to the resulting downwash at the respective collocation points

$$\boldsymbol{w}_{\mathrm{j}}(k) = \left(\boldsymbol{D}^{1}_{\mathrm{jk}} + jk\,\boldsymbol{D}^{2}_{\mathrm{jk}}\right)\,\boldsymbol{d}_{\mathrm{k}}(k)\,. \tag{18}$$

For the i'th panel, these matrices are defined as

$$\boldsymbol{D}^{1}_{\mathrm{jk},i} = \begin{bmatrix} 0 & 1 \end{bmatrix} \tag{19}$$

$$\boldsymbol{D}^{2}_{\mathrm{jk},i} = \frac{2}{\bar{c}} \begin{bmatrix} -1 & c_{\mathrm{i}}/4 \end{bmatrix}. \tag{20}$$

Thus, in contrast to pure heave displacements, pitch displacements induce downwash at the collocation point as indicated by Equation 19. Similarly, Equation 20 indicates that both heave and pitch displacement rates lead to downwash at the collocation point as well.
Lastly, the generalized aerodynamic matrix (GAM) $\boldsymbol{Q}_{\mathrm{hh}}(k)$ can be obtained. This frequency-dependent matrix maps rigid-body modes $\dot{\boldsymbol{\eta}}_{\mathrm{b}} = \left[\,\dot{V}_{\mathrm{b}}^{\mathsf{T}}\;\dot{\Omega}_{\mathrm{b}}^{\mathsf{T}}\,\right]^{\mathsf{T}}$ and flexible modes $\boldsymbol{\eta}_{\mathrm{f}}$ to the resulting aerodynamic rigid-body forces and moments as well as modal forces. Let $\boldsymbol{\Phi}_{\mathrm{gh}} = \begin{bmatrix}\boldsymbol{\Phi}_{\mathrm{gb}} & \boldsymbol{\Phi}_{\mathrm{gf}}\end{bmatrix}$, then the resulting forces and moments are given by

$$\begin{bmatrix} \boldsymbol{F}^{\mathrm{A}}_{\mathrm{b}} \\ \boldsymbol{M}^{\mathrm{A}}_{\mathrm{b}} \\ \boldsymbol{F}^{\mathrm{M}}_{\mathrm{f}} \end{bmatrix} = q_\infty \underbrace{\boldsymbol{\Phi}^{\mathsf{T}}_{\mathrm{gh}}\,\boldsymbol{T}^{\mathsf{T}}_{\mathrm{kg}}\,\boldsymbol{S}_{\mathrm{kj}}\,\boldsymbol{Q}_{\mathrm{jj}}\,\left(\boldsymbol{D}^{1}_{\mathrm{jk}} + jk\,\boldsymbol{D}^{2}_{\mathrm{jk}}\right)\,\boldsymbol{T}_{\mathrm{kg}}\,\boldsymbol{\Phi}_{\mathrm{gh}}}_{\boldsymbol{Q}_{\mathrm{hh}}(k)} \begin{bmatrix} \dot{\boldsymbol{\eta}}_{\mathrm{b}} \\ \boldsymbol{\eta}_{\mathrm{f}} \end{bmatrix}. \tag{21}$$

Here, $\boldsymbol{S}_{\mathrm{kj}}$ denotes the load transformation matrix that consists of block-diagonal entries of the individual panel area S_i and the individual panel area multiplied by the quarter chord length $S_i \cdot c_i/4$. It transforms the pressure obtained at each panel to the resulting z-force and pitching moment at the panel midpoint. Control surface deflections $\boldsymbol{\eta}_{\mathrm{x}}$ can be included with a modal matrix $\boldsymbol{\Phi}_{\mathrm{kx}}$ defined by rigid-body rotations and small angle approximations

$$\boldsymbol{d}_{\mathrm{k}} = \boldsymbol{\Phi}_{\mathrm{kx}}\,\boldsymbol{\eta}_{\mathrm{x}}\,. \tag{22}$$

Thus, $\boldsymbol{\Phi}_{\mathrm{kx}}$ maps the control surface deflections to the resulting heave and pitch displacements of the control surface panels' midpoints. Equation 21 can be extended to include the control

surface modes as

$$\begin{bmatrix} \boldsymbol{F}_{\mathrm{b}}^{\mathrm{A}} \\ \boldsymbol{M}_{\mathrm{b}}^{\mathrm{A}} \\ \boldsymbol{F}_{\mathrm{f}}^{\mathrm{M}} \end{bmatrix} = q_\infty \, \boldsymbol{\Phi}_{\mathrm{gh}}^{\mathsf{T}} \, \boldsymbol{T}_{\mathrm{kg}}^{\mathsf{T}} \, \boldsymbol{S}_{\mathrm{kj}} \, \boldsymbol{Q}_{\mathrm{jj}} \, \left(\boldsymbol{D}_{\mathrm{jk}}^{1} + jk \, \boldsymbol{D}_{\mathrm{jk}}^{2} \right) \begin{bmatrix} \boldsymbol{T}_{\mathrm{kg}} \, \boldsymbol{\Phi}_{\mathrm{gh}} & \boldsymbol{\Phi}_{\mathrm{kx}} \end{bmatrix} \begin{bmatrix} \dot{\boldsymbol{\eta}}_{\mathrm{b}} \\ \boldsymbol{\eta}_{\mathrm{f}} \\ \boldsymbol{\eta}_{\mathrm{x}} \end{bmatrix} . \tag{23}$$

From here on, it will be assumed that $\boldsymbol{Q}_{\mathrm{hh}}(k)$ includes the control surface modes as shown above. The GAM describes the aerodynamic model for a set of discrete frequencies k. In order to make it applicable for time-domain simulations, a rational function approximation (RFA) [38] has to be performed. To this end, a least-squares fit of the individual GAMs is performed in the frequency domain to obtain a continuous transfer function

$$\boldsymbol{Q}_{\mathrm{hh}}(s_k) = \boldsymbol{Q}_{\mathrm{hh}}^{0} + \boldsymbol{Q}_{\mathrm{hh}}^{1} \, s_k + \boldsymbol{Q}_{\mathrm{hh}}^{2} \, s_k^2 + \sum_{i=1}^{n_p} \boldsymbol{Q}_{\mathrm{hh}}^{\mathrm{L_i}} \, \frac{s_k}{s_k + p_i} \tag{24}$$

depending on the reduced frequency Laplace variable

$$s_k = \frac{\bar{c}}{2 \, V_{\mathrm{TAS}}} \, s. \tag{25}$$

The n_p lag poles are chosen in an iterative process to obtain a good fit. For the G-Flights Dimona, two poles at $p_1 = 0.075$ and $p_2 = 0.4$ were selected. The resulting fit is depicted in Figure 8 for the transfer functions of first symmetric wing bending mode and elevator deflection to Z-force. Apart from minor deviations at high frequencies, a good fit is obtained. The delayed

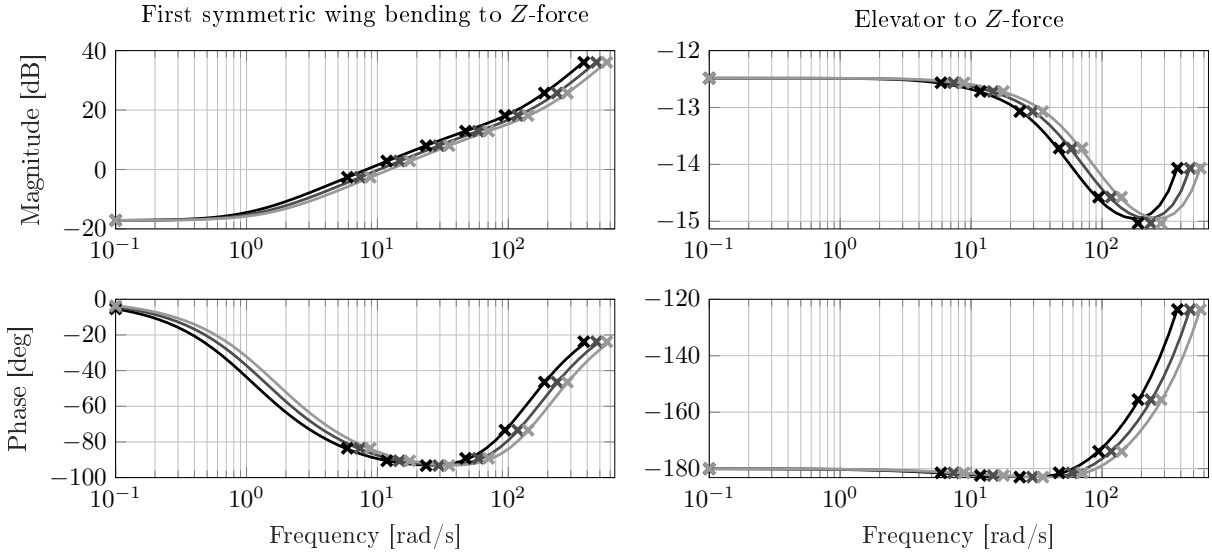

Figure 8: Rational function approximation of the transfer functions from first symmetric wing bending mode and elevator deflection to Z-force at 20 m/s (—), 25 m/s (—), and 30 m/s (—)

onset of unsteady effects with increasing airspeed indicates linear parameter-varying behavior. This is explained by the poles' dependence on airspeed in the actual frequency domain [36]

$$p_i^* = \frac{2 \, V_{\mathrm{TAS}} \, p_i}{\bar{c}} \, . \tag{26}$$

An early onset of unsteady effects in the transfer function from the first symmetric wing bending mode to the Z-force is noticeable, although the magnitudes are relatively low compared to

those in e.g. [20]. The mode has a relatively high damping ratio of approximately 0.6 to 0.7 at reasonable cruise speeds. The onset of unsteady effects due to elevator deflections begins at approximately $4\,\mathrm{rad/s}$, i.e. reduced frequencies of $k = 0.02$ to $k = 0.03$.
The doublet lattice model described in this subsection could be extended to six degrees of freedom for each aerodynamic panel and each structural node through appropriate expansion of the relevant matrices [18]. Making use of a modified numerical integration and a cross-product formulation, the so-called enhanced DLM would be obtained [23, 39].

3.4 Combined Model of Quasi-Steady and Unsteady Aerodynamics

In order to combine the quasi-steady strip aerodynamics described in subsection 3.2 with the unsteady DLM aerodynamics of subsection 3.3, two requirements must be fulfilled: First, the unsteady loads need to be available at the neutral points of each strip. This would allow for the superposition of quasi-steady and unsteady forces and moments. Second, the DLM model has to be separated into its steady and unsteady parts so that only the unsteady component can be added to the quasi-steady strip aerodynamics. The first requirement is implicitly fulfilled by the structure of the DLM model since the aerodynamic loads at each structural node $\boldsymbol{P}_{\mathrm{g}}^{\mathrm{A}}$ can be obtained by simply omitting the multiplication with $\boldsymbol{\Phi}_{\mathrm{gh}}^{\mathsf{T}}$ in Equation 23. Since each structural node is assigned to precisely one aerodynamic strip, the unsteady loads can subsequently be transferred to strip's the neutral point and henceforth be superimposed with the quasi-steady forces and moments. The second requirement can be fulfilled with the so-called physical rational function approximation (PRFA) proposed in [18]. This modification of the conventional RFA is based on directly fitting the AIC matrices instead of the GAMs. Thus, no multiplication with the differentiation matrices is performed prior to the function approximation. The main drawback of this approach is the significantly increased size of the matrices involved in the least-squares fit. In order to keep the matrix dimensions for the fit as low as possible, the AIC matrices are still premultiplied with $\boldsymbol{T}_{\mathrm{kg}}^{\mathsf{T}}\,\boldsymbol{S}_{\mathrm{kj}}$ to obtain

$$\boldsymbol{Q}_{\mathrm{gj}}(k) = \boldsymbol{T}_{\mathrm{kg}}^{\mathsf{T}}\,\boldsymbol{S}_{\mathrm{kj}}\,\boldsymbol{Q}_{\mathrm{jj}}(k)\,. \tag{27}$$

The PRFA is then given by

$$\boldsymbol{Q}_{\mathrm{gj}}(k) = \boldsymbol{Q}_{\mathrm{gj}}^{0} + \boldsymbol{Q}_{\mathrm{gj}}^{1}\,s_k + \sum_{i=1}^{n_p} \boldsymbol{Q}_{\mathrm{gj}}^{\mathrm{L_i}}\,\frac{s_k}{s_k + p_i}\,. \tag{28}$$

Now a distinction between the different components of the DLM model is possible: The steady part is given by $\boldsymbol{Q}_{\mathrm{gj}}^{0}$, added mass effects are represented by $\boldsymbol{Q}_{\mathrm{gj}}^{1}$, and the lag behavior is modeled by $\boldsymbol{Q}_{\mathrm{gj}}^{\mathrm{L_i}}$. Note the absence of the acceleration term $\boldsymbol{Q}_{\mathrm{gj}}^{2}$ in contrast to the conventional RFA in Equation 24. This term would be recovered by multiplication with the differentiation matrices to obtain the GAM as shown in [18, 36]. The same pole locations that were chosen for the conventional RFA were also used for the PRFA.

For implementation in the time-domain simulation model, the lag dynamics are represented by the state-space model [18]

$$\begin{aligned} \dot{\boldsymbol{x}}_L &= \boldsymbol{A}\left(\tfrac{V_\infty}{\bar{c}/2}\right)\boldsymbol{x}_L + \boldsymbol{B}\,\dot{\boldsymbol{w}}_{\mathrm{j}} \\ \boldsymbol{P}_{\mathrm{g}}^{\mathrm{Lag}} &= \boldsymbol{C}\,\boldsymbol{x}_L \end{aligned} \tag{29}$$

with

$$\begin{aligned}\boldsymbol{A} &= \operatorname{diag}\left(\begin{bmatrix}-p_1\,\boldsymbol{I} & \dots & -p_{n_p}\,\boldsymbol{I}\end{bmatrix}\right)\\ \boldsymbol{B} &= \begin{bmatrix}\boldsymbol{I} & \dots & \boldsymbol{I}\end{bmatrix}^{\mathsf{T}}\\ \boldsymbol{C} &= \begin{bmatrix}\boldsymbol{Q}_{\mathrm{gj}}^{\mathrm{L_1}} & \dots & \boldsymbol{Q}_{\mathrm{gj}}^{\mathrm{L_{np}}}\end{bmatrix},\end{aligned}$$

where $\boldsymbol{I}$ is an identity matrix of dimension $n_{\mathrm{panels}} \times n_{\mathrm{panels}}$. This state space model is usually of high dimension with $n_p \cdot n_{\mathrm{panels}}$ states and n_{panels} inputs. Nevertheless, a relatively efficient implementation can be achieved by exploiting the pronounced sparsity pattern of $\boldsymbol{A}$ and $\boldsymbol{B}$. The loads at each structural node determined by the DLM model are given by

$$\boldsymbol{P}_{\mathrm{g}}^{\mathrm{A}} = \bar{q}(\underbrace{\boldsymbol{Q}_{\mathrm{gj}}^{0}\,\boldsymbol{w}_{\mathrm{j}}}_{\text{steady}} + \underbrace{\boldsymbol{Q}_{\mathrm{gj}}^{1}\left(\tfrac{\bar{c}/2}{V_\infty}\right)\,\dot{\boldsymbol{w}}_{\mathrm{j}}}_{\text{added mass}} + \underbrace{\boldsymbol{C}\,\boldsymbol{x}_L(\dot{\boldsymbol{w}}_{\mathrm{j}})}_{\text{lag}})\,. \tag{30}$$

To implement the unsteady aerodynamics model, only the added mass and lag term are considered. The steady part is replaced by the quasi-steady model. The components of the downwash derivative are given by

$$\dot{\boldsymbol{w}}_{\mathrm{j}} = \begin{cases}\boldsymbol{D}_{\mathrm{jk}}^{2}\,\boldsymbol{T}_{\mathrm{kg}}\,\boldsymbol{\Phi}_{\mathrm{gb}}\left(\tfrac{\bar{c}/2}{V_\infty}\right)\,\ddot{\boldsymbol{\eta}}_{\mathrm{b}}\\ +\boldsymbol{D}_{\mathrm{jk}}^{1}\,\boldsymbol{\Phi}_{\mathrm{kx}}\,\dot{\boldsymbol{\eta}}_{\mathrm{x}}\\ +\boldsymbol{D}_{\mathrm{jk}}^{2}\,\boldsymbol{\Phi}_{\mathrm{kx}}\left(\tfrac{\bar{c}/2}{V_\infty}\right)\,\ddot{\boldsymbol{\eta}}_{\mathrm{x}}\\ +\boldsymbol{D}_{\mathrm{jk}}^{1}\,\boldsymbol{T}_{\mathrm{kg}}\,\boldsymbol{\Phi}_{\mathrm{gf}}\,\dot{\boldsymbol{\eta}}_{\mathrm{f}}\\ +\boldsymbol{D}_{\mathrm{jk}}^{2}\,\boldsymbol{T}_{\mathrm{kg}}\,\boldsymbol{\Phi}_{\mathrm{gf}}\left(\tfrac{\bar{c}/2}{V_\infty}\right)\,\ddot{\boldsymbol{\eta}}_{\mathrm{f}}\\ +\dot{\boldsymbol{w}}_{\mathrm{j}}^{\mathrm{G}}\,,\end{cases} \tag{31}$$

where $\dot{\boldsymbol{w}}_{\mathrm{j}}^{\mathrm{G}}$ is the gust induced downwash derivative. It can be conveniently defined in the time-domain for 1-cos gusts as described in [18]. The relative position of the aerodynamic panels' collocation points w.r.t the gust is given by

$$\boldsymbol{x}_{\mathrm{j}}^{\mathrm{G}}(t) = \boldsymbol{x}_{\mathrm{j}} + 2\,H - V_{\mathrm{TAS}}\,t\,, \tag{32}$$

where $\boldsymbol{x}_{\mathrm{j}}$ denotes the collocation points' positions and H is the gust gradient. The gust downwash derivative is then defined as

$$\dot{\boldsymbol{w}}_{\mathrm{j}}^{\mathrm{G}}(t) = \begin{cases}-\frac{\pi\,V^{\mathrm{G}}}{2\,H}\sin\left(\pi\,\frac{\boldsymbol{x}_{\mathrm{j}}^{\mathrm{G}}(t)}{H}\right) & \text{for } 0 < \boldsymbol{x}_{\mathrm{j}}^{\mathrm{G}} < 2\,H\\ 0 & \text{otherwise}\end{cases} \tag{33}$$

with the gust amplitude V^{G}.

With the definitions above, the outputs of the unsteady model are given by the loads due to added mass effects $\boldsymbol{P}_{\mathrm{g}}^{\mathrm{A,am}}$ and lag effects $\boldsymbol{P}_{\mathrm{g}}^{\mathrm{A,lag}}$. After transferring them from the structural nodes to the strips' neutral points, they are superimposed with the quasi-steady loads $\boldsymbol{P}_{\mathrm{n}}^{\mathrm{A,qs}}$ to obtain the distributed aerodynamic forces and moments acting at the neutral points

$$\boldsymbol{P}_{\mathrm{n}}^{\mathrm{A}} = \boldsymbol{P}_{\mathrm{n}}^{\mathrm{A,qs}} + \boldsymbol{P}_{\mathrm{n}}^{\mathrm{A,am}} + \boldsymbol{P}_{\mathrm{n}}^{\mathrm{A,lag}}\,. \tag{34}$$

Since the lag term inherently models delayed downwash effects, it replaces the delay of the quasi-steady downwash model Equation 9. It is thus excluded from the quasi-steady strip aerodynamics such that delayed downwash effects are represented by the corresponding lag forces

acting at the neutral points of the tailplane strips. The distributed aerodynamic forces and moments are summed up to yield the aerodynamic forces $\boldsymbol{F}_{\mathrm{b}}^{\mathrm{A}}$ and moments $\boldsymbol{M}_{\mathrm{b}}^{\mathrm{A}}$ for the rigid-body equations of motion in Equation 2 and Equation 3, respectively. The modal forces for the structural dynamics in Equation 4 are determined by multiplying the aerodynamic loads acting at the structural nodes with the transposed flexible modal matrix

$$\boldsymbol{F}_{\mathrm{f}}^{\mathrm{M}} = \boldsymbol{\Phi}_{\mathrm{gf}}^{\mathsf{T}} \, \boldsymbol{P}_{\mathrm{g}}^{\mathrm{A}} \, . \tag{35}$$

It should be noted that differences in the aerodynamic grids of the quasi-steady strip model and the unsteady panel model lead to a model mismatch when simulating very short gusts. In the quasi-steady strip model, a gust acts directly at the neutral point as soon as it is reached. In contrast, in the DLM model, a gust acts at each panel's collocation point while traveling over the lifting surfaces. This results in a possible mismatch between the time-dependent reactions of the two models. This effect can be largely mitigated by shifting the gust downwash derivative $\dot{\boldsymbol{w}}_{\mathrm{j}}^{\mathrm{G}}(t)$ by $\Delta t = \bar{c}/(2\,V_{\mathrm{TAS}})$ in time as illustrated in Figure 9. This implies that the gust has already traveled half the mean chord of the panel model when it reaches the leading edge of the strip model. Comparisons of the quasi-steady model with a steady VLM model on the same grid as the DLM model indicated that this approach yields satisfactory results by correctly matching the forces in reaction to gusts, except when high-frequency gusts with very short time scales are considered.

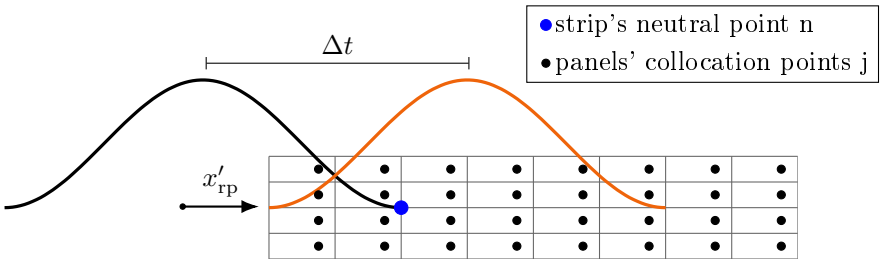

Figure 9: Schematic illustration of the time shift between the gusts of the quasi-steady model (——) and the unsteady model (——) to achieve force matching in time

4 COMPARISON OF QUASI-STEADY AND UNSTEADY SIMULATIONS

This section analyzes the impact of unsteady aerodynamic effects on the slightly flexible G-Flights Dimona. Prior to analyzing the simulations, a new parameter estimation is performed to adapt the quasi-steady aerodynamic model after its combination with the unsteady DLM model. This adapted unsteady model is then compared to the purely quasi-steady model in simulations of maneuvers and gusts over a wide range of reduced frequencies.

4.1 Quasi-Steady Parameter Estimation

The parameter estimation follows the approach that has previously been taken to estimate the parameters of the quasi-steady strip aerodynamics model [26]. Therein, the distributions of the quasi-steady control and stability derivatives were adapted by scaling the initial distributions with scaling factors. The same data set consisting of maneuvers to excite the rigid-body dynamics is used here. For this reason, only the parameters of the quasi-steady are adapted while the unsteady aerodynamics remain unchanged. Consistency of the quasi-steady strip model and the unsteady DLM model can thus be ensured. Additionally, a good match between the combined model and flight test data in the quasi-steady regime can be achieved.

The estimation is performed with the in-house tool DAVIS, which is based on the output-error method in the time-domain and maximum likelihood-estimation [32]. The estimation parameters comprise linear scaling factors of the zero coefficient, stability derivative, and control derivative distributions as well as additional parameters of the downwash and fuselage [26].

$$\boldsymbol{\Theta} = \left[k\_C_{D_0} \;\; k\_C_{Y_\beta} \;\; k\_C_{L_0,\text{wing}} \;\; k\_C_{L_\alpha,\text{wing}} \;\; k\_C_{L_\alpha,\text{htp}} \;\; k\_C_{L_{\boldsymbol{\eta}_{\text{x},i}}} \;\; \partial\epsilon_T/\partial\alpha \;\; \partial\epsilon_T/\partial\eta_{\text{x},i_\text{f}} \;\; C_{l_{0,\text{fuse}}} \;\; C_{m_{0,\text{fuse}}} \right]^\mathsf{T} . \tag{36}$$

The criteria for the estimation are selected from standard measurement outputs of the rigid body motion

$$\boldsymbol{y} = \left[\; V_\text{TAS} \;\; \dot{p} \;\; \dot{q} \;\; \dot{r} \;\; p \;\; q \;\; r \;\; \phi \;\; \theta \;\; \psi \;\; u \;\; v \;\; w \;\; a_x \;\; a_y \;\; a_z \; \right]^\mathsf{T} . \tag{37}$$

Matching plots of the identification result are shown in the appendix in Figure 13. Apart from some deviations due to model deficiencies and undetected atmospheric disturbances, a good overall identification result similar to the identification of the quasi-steady model in [26] is achieved. Especially the fast dynamics are matched well. This result indicates that the combined quasi-steady/unsteady model is plausible and in good agreement with quasi-steady flight test data. Time-dependent downwash effects that were previously explicitly modeled in the quasi-steady aerodynamics are now represented by the DLM model. The final estimates are listed in Table 2, where initial values of 1 represent the scalings obtained from the identification of the purely quasi-steady model in [26]. Predominantly, the angle of attack derivative

Table 2: Quasi-steady parameter estimates

Parameter	Initial value	Final value	Rel. std. deviation [%]
$k\_C_{D_0}$	1	0.99	1.87
$k\_C_{Y_\beta}$	1	1	0.79
$k\_C_{L_0,\text{wing}}$	1	1.36	2.49
$k\_C_{L_\alpha,\text{wing}}$	1	0.83	0.85
$k\_C_{L_{\eta_{\text{x,fl}}}}$	1	0.88	1.08
$k\_C_{L_{\eta_{\text{x,a,in}}}}$	1	0.85	1.08
$k\_C_{L_{\eta_{\text{x,x,a,out}}}}$	1	0.87	0.97
$k\_C_{L_\alpha,\text{htp}}$	1	1.26	1.74
$k\_C_{L_{\eta_{\text{x},e}}}$	1	1.14	0.72
$k\_C_{Y_{\eta_{\text{x},r}}}$	1	1.02	1.29
$\partial\epsilon_T/\partial\alpha$	0.411	0.561	1.95
$\partial\epsilon_T/\partial\eta_{\text{x},i_\text{f}}$	0.0248	0.017	2.24
$C_{l_{0,\text{fuse}}}$	-0.0017	-0.0017	0.93
$C_{m_{0,\text{fuse}}}$	-0.0356	-0.0378	6.39

distributions of the wing and the horizontal tailplane, the corresponding control surfaces, and the partial downwash derivatives are adapted. Parameters of the fuselage aerodynamics and the yawing motion are hardly altered. This indicates a reasonable identification since unsteady effects are not implemented for these parameters. All estimates are reasonably close to the initial values and have low relative standard deviations. The adaptations of the lift scalings are attributed to the additional unsteady forces acting on the wing and the horizontal tailplane. The change in downwash derivatives indicates an adjustment required to match the flight test data with the time-dependent downwash effects now included in the DLM model. The adapted model obtained in this subsection demonstrates overall satisfying behavior and is hence used for subsequent simulation studies.

4.2 Simulation Studies of Maneuvers and Gust Encounters

The combined unsteady model is compared to the purely quasi-steady model in simulations studies. A wide range of reduced frequencies is considered to evaluate the impact of unsteady effects on the overall flight dynamic and aeroelastic behavior.
To evaluate unsteady effects in the rigid-body frequency range, an elevator 3-2-1-1 maneuver is simulated to excite the short period dynamics. The maneuver is executed at $V_{\mathrm{TAS}} = 22\,\mathrm{m/s}$ where the short period mode reaches its maximum frequency of $\omega_{\mathrm{n,SP}} = 7.02\,\mathrm{rad/s}$. Note that the short period is overall highly damped with a damping ratio of $\zeta = 0.95$ at $22\,\mathrm{m/s}$. The time step for the 3-2-1-1 input is approximated by $\Delta t_{3211} = \pi/(2\,\omega_{\mathrm{n,SP}}) \approx 0.22\,\mathrm{s}$ and the elevator deflection is chosen such that $\Delta\alpha \approx 3° \ldots 4°$ is achieved [32]. The simulation results are shown in Figure 10. No significant differences between the quasi-steady and the unsteady

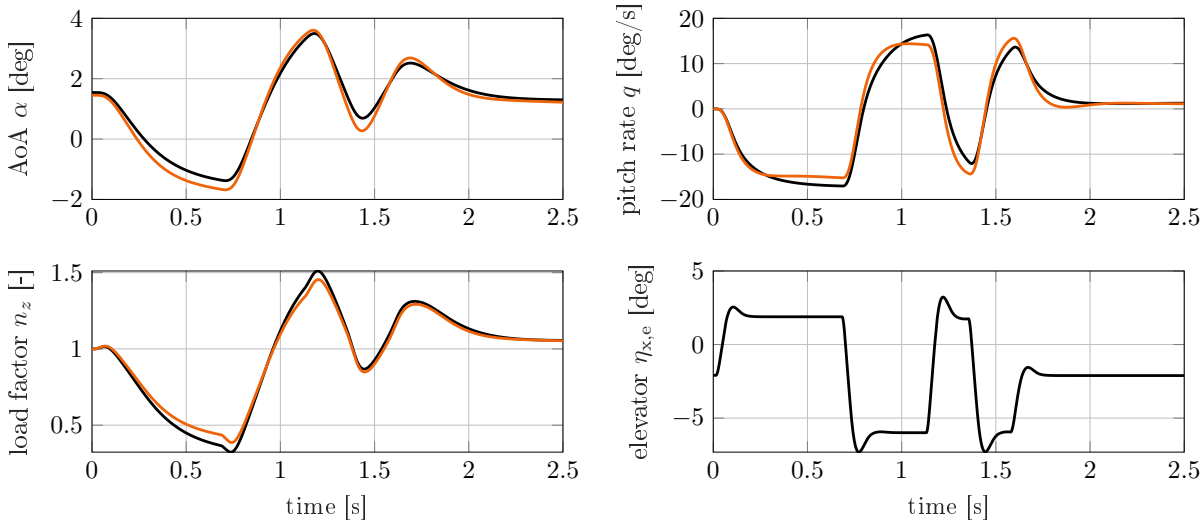

Figure 10: Quasi-steady (——) and unsteady (——) simulations of an elevator 3-2-1-1 maneuver at $V_{\mathrm{TAS}} = 22\,\mathrm{m/s}$

model are observed. This is considered reasonable for the slightly flexible Dimona at $k = 0.05$. The existing differences in the pitch dynamics can mostly be attributed to the adaptation of the quasi-steady parameters.

In order to excite high frequency aeroelastic dynamics, an elevator sine sweep from 1 Hz to 6 Hz executed at $V_{\mathrm{TAS}} = 20\,\mathrm{m/s}$ is considered. The resulting wing tip accelerations are depicted in Figure 11. Here, the excitation of the first wing bending mode is visible at $t \approx 5\,\mathrm{s}$. The differences between the combined unsteady model and the quasi-steady model at $k \approx 0.1$ are most likely still dominated by the quasi-steady parameter adaptation. At $k \approx 0.2$, a phase shift and a decrease in amplitude become evident. The unsteady aerodynamics result in a significant phase shift and decrease in amplitude of the wing tip acceleration at $k \approx 0.3$. Note that $k \approx 0.3$ is reached with a rather low airspeed of $V_{\mathrm{TAS}} = 20\,\mathrm{m/s}$ and an elevator frequency of 6 Hz, which is close to the maximum actuator bandwidth of 6.74 Hz. Thus, higher reduced frequencies will hardly be reached with maneuvers. While the impact of the unsteady aerodynamics is clearly visible in the aeroelastic frequency range, there remains a distinct separation between these frequencies and those of the rigid-body dynamics so that unsteady effects hardly affect the rigid-body dynamics.

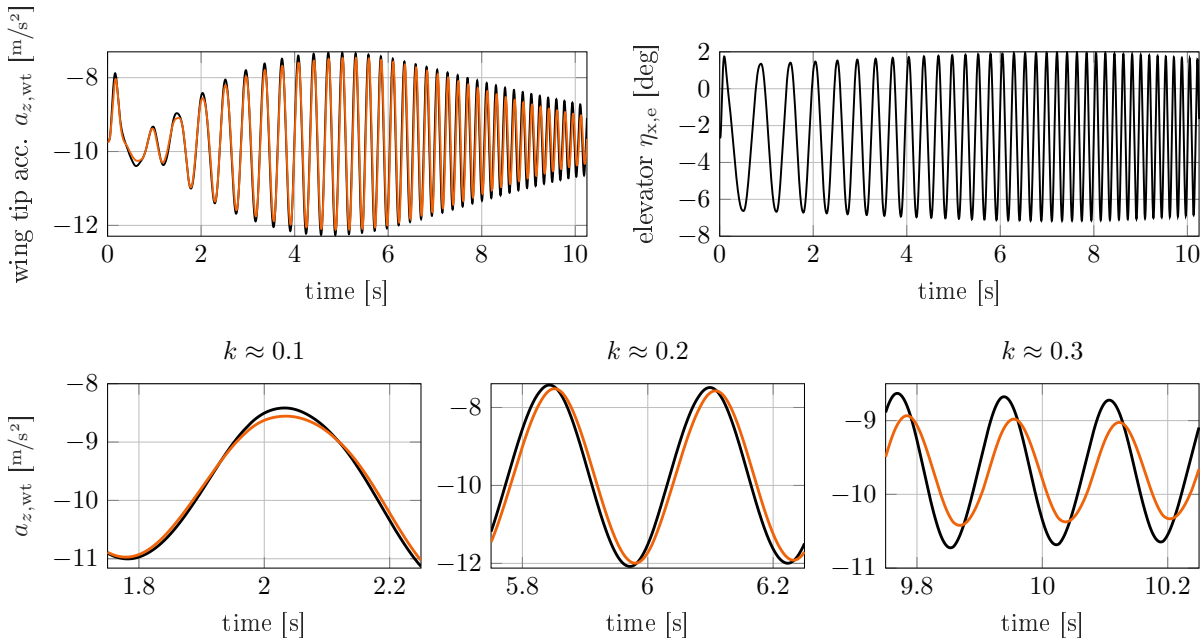

Figure 11: Quasi-steady (—) and unsteady (—) simulations of an elevator sine sweep from 1 Hz to 6 Hz at $V_{\mathrm{TAS}} = 20\,\mathrm{m/s}$

The most notable impact of unsteady effects is expected during gust encounters. To this end, three 1-cos discrete gusts with decreasing gust lengths are simulated at a cruise speed of $V_{\mathrm{TAS}} = 25\,\mathrm{m/s}$. Since 1-cos gusts are especially relevant in loads analysis, the wing root bending moment (WRBM) is considered to evaluate the unsteady effects. The simulation results of the three gusts are depicted in Figure 12. For $k = 0.2$, the impact of unsteady aerodynamics

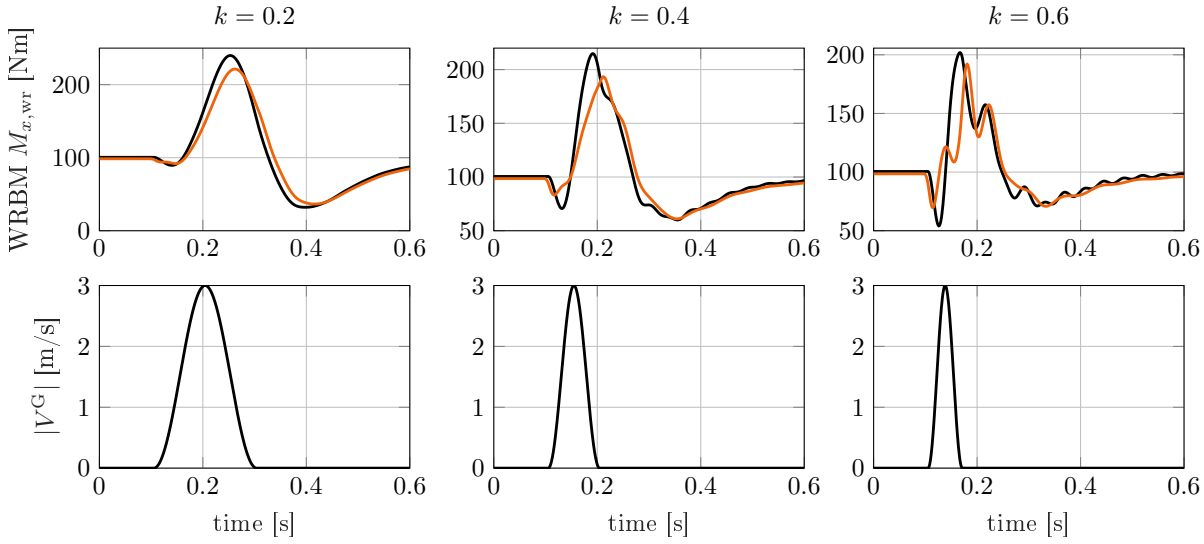

Figure 12: Quasi-steady (—) and unsteady (—) simulations of gust encounters at four different reduced frequencies with $V_{\mathrm{TAS}} = 25\,\mathrm{m/s}$

is visible by means of a phase shift, and qualitative similarities to $k \approx 0.2$ in Figure 11 can be observed. The effects become more pronounced at higher frequencies with a stronger phase shift and decrease of the maximum WRBM at $k = 0.4$. The slightly earlier reaction of the

unsteady WRBM due to added mass effects is visible. Lastly, the most significant impact of unsteady effects is observed for $k = 0.6$, showing a clear difference in load progression. It is thus confirmed that unsteady effects become especially relevant for short gusts. The resulting time delays and deviations in WRBM amplitude can be of importance when considering gust load analysis and load control.

It can be concluded that the purely quasi-steady model captures the essential dynamics with reduced frequencies of $k < 0.2$ well. At higher frequencies, unsteady effects influence the dynamics significantly. They result in phase-shifts, changes in amplitude, and delays due to the added mass and lag forces. For the slightly flexible G-Flights Dimona, these reduced frequencies are not reached during conventional maneuvering flight. It is thus concluded that unsteady aerodynamics will most likely not have to be considered for classical controller design. However, they can become relevant during loads analysis and control of short gusts, where high-frequency control surface deflections are required.

5 CONCLUSION

The modeling and analysis of unsteady aerodynamics for a slightly flexible $25\,\mathrm{kg}$ unmanned aircraft was presented. An identified high-fidelity quasi-steady strip aerodynamics model was combined with DLM unsteady aerodynamics by exploiting the structure of the physical rational function approximation. In this way, it is possible to differentiate between the steady and unsteady parts of the DLM model and the steady part can be replaced by the high-fidelity quasi-steady model. The combined aerodynamics were integrated into a modeling framework for flexible aircraft, using linear structural dynamics and nonlinear equations of motion based on the practical mean-axes formulation. The quasi-steady part of the combined model was newly adapted with a parameter estimation based on quasi-steady flight test data. Overall, a good match with the flight test data was obtained, ensuring consistency of the models. Simulation studies of maneuvers and gusts exciting the rigid-body and aeroelastic dynamics over a wide range of reduced frequencies were performed. Significant differences to purely quasi-steady simulations were observed for maneuvers at relatively high reduced frequencies in the aeroelastic frequency range close to the actuator bandwidth, while the rigid-body dynamics remained mostly unaffected. The strongest influence of the unsteady aerodynamic effects was observed during gust encounters. The response of the wing root bending moment was significantly altered for short gusts. It was concluded that unsteady effects are most likely negligible for classical controller design of the unmanned slightly flexible aircraft. However, they could be relevant during loads analysis and control of short gusts.

6 APPENDIX: SYSTEM IDENTIFICATION MATCHING PLOTS

Matching plots for the system identification results of the quasi-steady parameters for the combined model.

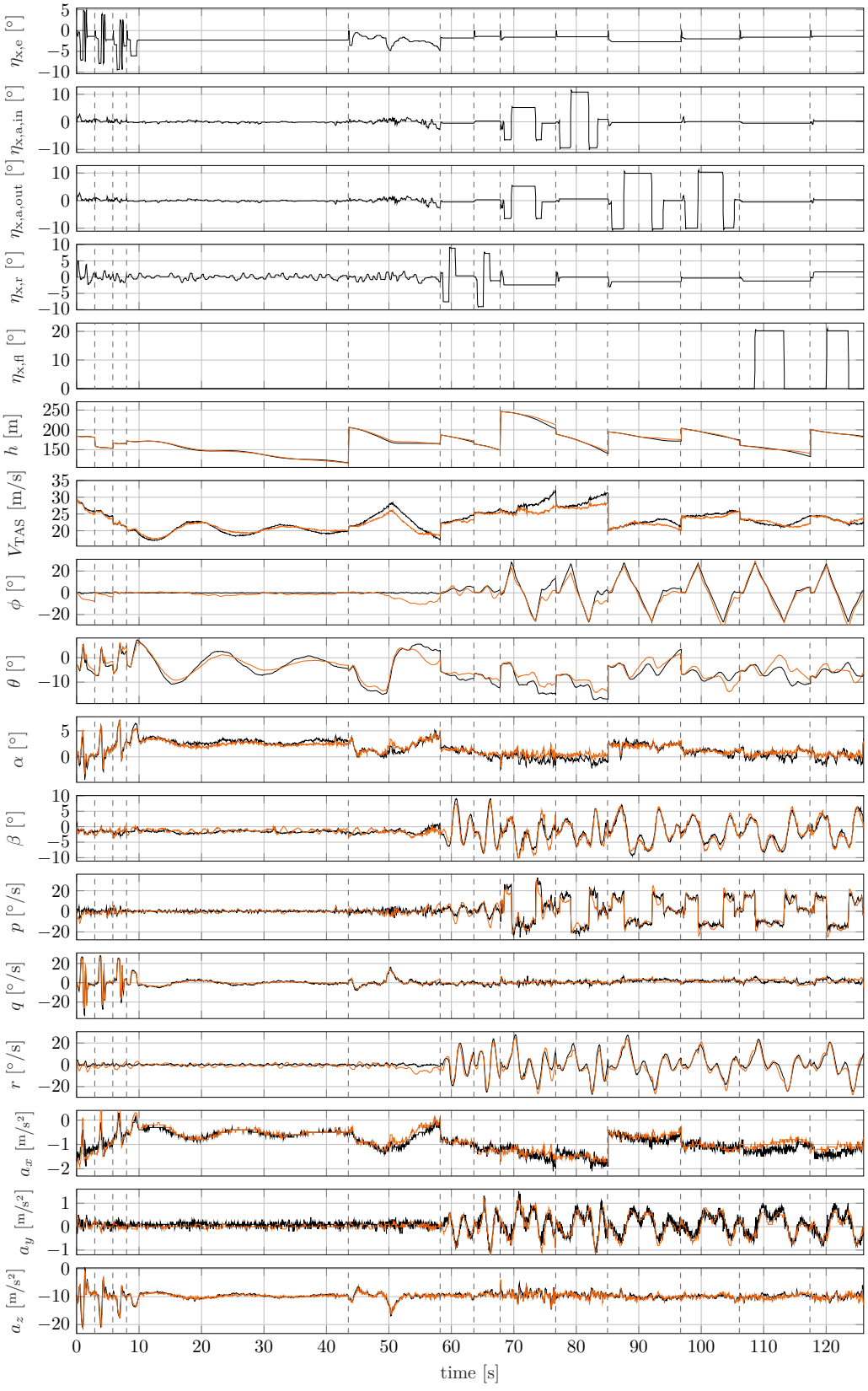

Figure 13: System identification results comparing flight test data (—) and simulation data (—)

7 REFERENCES

[1] Wagner, H. (1925). Über die entstehung des dynamischen auftriebes von tragflügeln. *ZAMM - Zeitschrift für Angewandte Mathematik und Mechanik*, 5(1), 17–35. doi:10.1002/zamm.19250050103.

[2] Küssner, H. G. (1936). Zusammenfassender bericht über den instationären auftrieb von flügeln. *Luftfahrtforschung*, 13(12), 410–424.

[3] Tucker, P. G. (2013). *Unsteady computational fluid dynamics in aeronautics*, vol. 104. Springer Science & Business Media.

[4] de C. Henshaw, M., Badcock, K., Vio, G., et al. (2007). Non-linear aeroelastic prediction for aircraft applications. *Progress in Aerospace Sciences*, 43(4–6), 65–137. ISSN 0376-0421. doi:10.1016/j.paerosci.2007.05.002.

[5] Theodorsen, T. (1949). General theory of aerodynamic instability and the mechanism of flutter. Tech. rep., National Advisory Committee for Aeronautics. Langley Aeronautical Lab. Langley Field, VA, United States.

[6] Yates Jr, E. C. (1966). Modified-strip-analysis method for predicting wing flutter at subsonic to hypersonic speeds. *Journal of Aircraft*, 3(1), 25–29.

[7] Rodden, W. P. and Stahl, B. (1969). A strip method for prediction of damping in subsonic wind tunnel andflight flutter tests. *Journal of Aircraft*, 6(1), 9–17. ISSN 1533-3868. doi:10.2514/3.43994.

[8] Leishman, J. G. (1994). Unsteady lift of a flapped airfoil by indicial concepts. *Journal of Aircraft*, 31(2), 288–297. ISSN 1533-3868. doi:10.2514/3.46486.

[9] Andrews, S. P. (2011). *Modelling and simulation of flexible aircraft: handling qualities with active load control*. Ph.D. thesis, Cranfield University.

[10] Silvestre, F. J. and Luckner, R. (2015). Experimental validation of a flight simulation model for slightly flexible aircraft. *AIAA Journal*, 53(12), 3620–3636. ISSN 1533-385X. doi:10.2514/1.j054023.

[11] Beyer, Y., Cavaliere, D., Bramsiepe, K., et al. (2023). An aeroelastic flight dynamics model for gust load alleviation of energy-efficient passenger airplanes. In *AIAA AVIATION 2023 Forum*. American Institute of Aeronautics and Astronautics. doi:10.2514/6.2023-4452.

[12] Albano, E. and Rodden, W. (1969). A doublet-lattice method for calculating lift distributions on oscillating surfaces in subsonic flows. *Journal of Aircraft*, 7(2), 279–285.

[13] Kalman, T. P., Rodden, W. P., and Giesing, J. P. (1971). Application of the doublet-lattice method to nonplanar configurations in subsonic flow. *Journal of Aircraft*, 8(6), 406–413. ISSN 1533-3868. doi:10.2514/3.59117.

[14] Rodden, W. P., Giesing, J., and Kalman, T. (1972). Refinement of the nonplanar aspects of the subsonic doublet-lattice lifting surface method. *Journal of Aircraft*, 9(1), 69–73.

[15] Rodden, W. P., Taylor, P. F., and McIntosh, S. C. (1998). Further refinement of the subsonic doublet-lattice method. *Journal of Aircraft*, 35(5), 720–727. ISSN 1533-3868. doi:10.2514/2.2382.

[16] Rodden, W. P., Taylor, P. F., and McIntosh, S. (1999). Improvements to the doublet-lattice method in msc/nastran. *MacNeal-Schwendler Corp., Technical Rept., Los Angeles*.

[17] Kier, T. (2005). Comparison of unsteady aerodynamic modelling methodologies with respect to flight loads analysis. In *AIAA Atmospheric Flight Mechanics Conference and Exhibit*. p. 6027.

[18] Kier, T. and Looye, G. (2009). Unifying manoeuvre and gust loads analysis. In *International Forum on Aeroelasticity and Structural Dynamics (IFASD)*.

[19] Kier, T. M. (2012). Aerodynamic modelling for integrated loads analysis models. In *Third Symposium in Simulation of Wing and Nacelle Stall, Braunschweig, Germany*.

[20] Kotikalpudi, A., Pfifer, H., and Balas, G. J. (2015). Unsteady aerodynamics modeling for a flexible unmanned air vehicle. In *AIAA Atmospheric Flight Mechanics Conference*. American Institute of Aeronautics and Astronautics. doi:10.2514/6.2015-2854.

[21] Takarics, B., Vanek, B., Kotikalpudi, A., et al. (2018). Flight control oriented bottom-up nonlinear modeling of aeroelastic vehicles. In *2018 IEEE Aerospace Conference*. IEEE. doi:10.1109/aero.2018.8396537.

[22] Wuestenhagen, M., Kier, T., Meddaikar, Y. M., et al. (2018). Aeroservoelastic modeling and analysis of a highly flexible flutter demonstrator. In *2018 Atmospheric Flight Mechanics Conference*. American Institute of Aeronautics and Astronautics. doi:10.2514/6.2018-3150.

[23] Kier, T. M. (2023). Comparing different potential flow methods for unsteady aerodynamic modelling of a flutter demonstrator aircraft. In *AIAA SciTech 2023 Forum*.

[24] Schmidt, D. K., Zhao, W., and Kapania, R. K. (2016). Flight-dynamics and flutter modeling and analyses of a flexible flying-wing drone - invited. In *AIAA Atmospheric Flight Mechanics Conference*. American Institute of Aeronautics and Astronautics. doi:10.2514/6.2016-1748.

[25] Herrmann, B., Theis, J., and Thielecke, F. (2022). System identification of a nonlinear uav model with distributed aerodynamics and flexible structure. In *CEAS EuroGNC 2022*.

[26] Herrmann, B., Theis, J., and Thielecke, F. (2023). Nonlinear system identification of a uav model with distributed aerodynamics and flexible structure. *CEAS Aeronautical Journal*, 14(3), 661–677. ISSN 1869-5590. doi:10.1007/s13272-023-00674-x.

[27] Luderer, O., Thielecke, F., Wagner, J., et al. (2023). Development and testing of a complementary sensor network for robust estimation of maneuver and gust loads. In *Deutscher Luft- und Raumfahrtkongress (DLRK 2023)*.

[28] Rieck, L., Herrmann, B., Thielecke, F., et al. (2023). Efficient quasi-linear model predictive control of a flexible aircraft based on laguerre functions. In *2023 American Control Conference (ACC)*. IEEE, pp. 2855–2860.

[29] Gonzalez, P., Starvorinus, G., Silvestre, F. J., et al. (2023). Tu-flex: A very-flexible flying demonstrator with a generic transport aircraft configuration. In *AIAA SCITECH 2023 Forum*. American Institute of Aeronautics and Astronautics. doi:10.2514/6.2023-1312.

[30] Henning, K., Montel, M., Köthe, A., et al. (2017). Experimentelle ermittlung der modalen strukturparameter eines skalierten flugversuchsträgers mittels low-cost sensoren. In *66. Deutscher Luft-und Raumfahrtkongress, (DLRK 2017)*. DLRK.

[31] Waszak, M. R. and Schmidt, D. K. (1988). Flight dynamics of aeroelastic vehicles. *Journal of Aircraft*, 25(6), 563–571. ISSN 1533-3868. doi:10.2514/3.45623.

[32] Jategaonkar, R. (2015). *Flight Vehicle System Identification*. American Institute of Aeronautics and Astronautics. ISBN 9781624102783.

[33] Schlichting, H. and Truckenbrodt, E. (1960). *Aerodynamik des Flugzeuges*. Springer Berlin Heidelberg. ISBN 9783642530463. doi:10.1007/978-3-642-53046-3.

[34] Brockhaus, R., Alles, W., and Luckner, R. (2011). *Flugregelung*. Springer Berlin Heidelberg. ISBN 9783642014437. doi:10.1007/978-3-642-01443-7.

[35] Nastran, M. S. C. (2004). Aeroelastic analysis user's guide. *CA, USA, Version*, 68.

[36] Kotikalpudi, A. (2017). *Robust flutter analysis for aeroservoelastic systems*. Ph.D. thesis, University of Minnesota.

[37] Harder, R. L. and Desmarais, R. N. (1972). Interpolation using surface splines. *Journal of Aircraft*, 9(2), 189–191. ISSN 1533-3868. doi:10.2514/3.44330.

[38] Roger, K. L. (1977). Airplane math modeling methods for active control design. In *Advisory Group for Aerospace Research and Development CP-228*.

[39] van Zyl, L. H. (2008). Unsteady panel method for complex configurations including wake modeling. *Journal of Aircraft*, 45(1), 276–285. ISSN 1533-3868. doi:10.2514/1.29267.

ACKNOWLEDGMENTS

This work was partly funded by the research project ”Integrated flight and loads control of very flexible aircraft for the multidisciplinary aircraft design of future climate-neutral aircraft” (FlexFuture), which is supported by the German Federal Ministry for Economic Affairs and Climate Action in the national LuFo VI-2 program. Any opinions, findings and conclusions expressed in this document are those of the authors and do not necessarily reflect the views of the other project partners.

Supported by:

on the basis of a decision
by the German Bundestag